Otani and colleagues explore the relationship between myocardial ^{11}C-DAG accumulation assessed by PET and left ventricular enlargement, systolic dysfunction, and humoral activation after myocardial infarction. . . . . ***Page 553***

Ribeiro and colleagues use ^{18}F-fluoro-L-DOPA PET to detect hyperfunctional pancreatic islet tissue and distinguish between the diffuse and focal forms of hyperinsulinism in infants. . . . . ***Page 560***

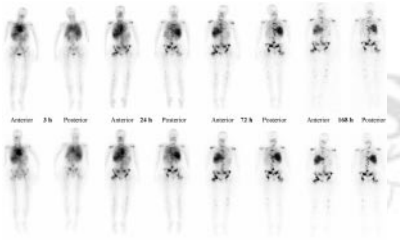

Akhtar and colleagues evaluate the scintigraphic imaging potential of ^{99m}Tc-ubiquicidin 29-41, a synthetic antimicrobial peptide fragment, for localizing foci of infection in human bone and soft tissues. . . . . ***Page 567***

Minutoli and colleagues report on the effect of timing differences on the reliability of ^{99m}Tc-MIBI SPECT imaging in differentiating neoplastic from nonneoplastic intraparenchymal cerebral hemorrhage. . . . . ***Page 574***

Hockaday and colleagues assess imaging and biodistribution data from a phase I/II trial of intracavitary ^{131}I-TM-601 in patients with recurrent high-grade glioma to determine whether this radiolabeled compound might be useful in estimating the extent of primary brain tumor. . . . . ***Page 580***

Kim and colleagues compare inline PET/CT with dedicated PET and with software fusion of independently acquired CT and PET scans for staging of recurrent colorectal cancer. . . . ***Page 587***

Beyer and colleagues report on the efficacy of several support structures and placements in reducing the likelihood of patient motion in the head and neck during whole-body PET/CT studies. . . ***Page 596***

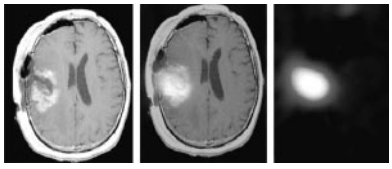

Halpern and colleagues characterize optimal lutetium orthosilicate PET imaging protocols to meet the challenges of lesion detection in obese patients. . . . ***Page 603***

Brix and colleagues use a phantom to assess the radiation exposure of patients undergoing whole-body ^{18}F-FDG PET/CT examinations at 4 hospitals with different tomographs and imaging protocols and describe possible strategies to reduce exposure while maintaining quality. . ***Page 608***

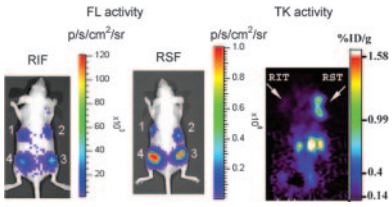

Parsey and colleagues investigate human biodistribution and dosimetry of the PET serotonin 1A antagonist ^{11}C-WAY100,635 and discuss the importance of human dosimetry studies in the development of new radiotracers. . ***Page 614***

Sharkey and colleagues describe the pharmacokinetics, dosimetry, and dose-limiting toxicity of a support protocol for patients with advanced medullary thyroid cancer, including humanized anticarcinoembryonic antigen or monoclonal antibody combined with doxorubicin and peripheral blood stem cell support. . . . . ***Page 620***

Vallabhajosula and colleagues compare the pharmacokinetics and biodistribution of ^{111}In- and ^{177}Lu-labeled J591 antibody in patients with prostate cancer and estimate the radiation dosimetry of ^{90}Y-J591 to assess the utility of ^{111}In as a chemical and biologic surrogate for ^{90}Y. . ***Page 634***

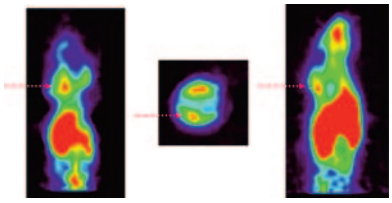

Shen and colleagues detail the patient-specific dosimetry of pretargeted ^{90}Y/^{111}In-DOTA-biotin after CC49 fusion protein in patients with metastatic gastrointestinal cancer. . . . . ***Page 642***

Lee and colleagues evaluate the feasibility of sodium-iodide (NIS) symporter gene imaging with radioiodide scintigraphy for assessing myocardial gene expression in a rat model by using a dual-gene adenovirus that expresses both NIS protein and enhanced green fluorescent protein. . . . . ***Page 652***

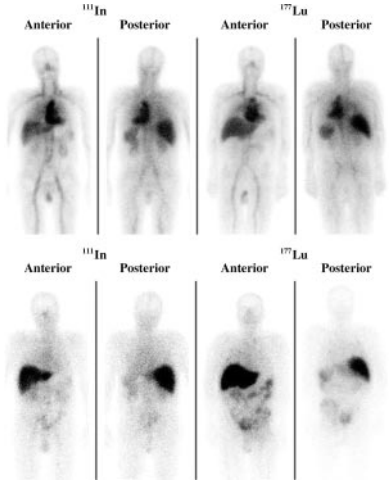

Yagle and colleagues investigate ^{18}F-annexin V binding to apoptotic tissues in a

model of chemically induced apoptosis in rat liver and discuss the potential of this radiolabeled protein for early, individualized PET assessment of clinical response to cancer therapy. . . . . *Page 658*

Wang and colleagues combine bioluminescence and microPET modalities to elucidate the utility of homeodomain protein SIRES bicistronic vectors for improved assessment of therapeutic gene expression based on reporter gene expression in living subjects. . . . . *Page 667*

Zhao and colleagues describe the intratumoral distribution of ^{18}F-FDG and compare it with regional expression levels of glucose transporters and hexokinase-II in a rat model of malignant tumor. . . . . *Page 675*

Vavere and Welch outline the biodistribution and microPET imaging characteristics of ^{45}Ti-transferrin in a mouse model to provide insight into the action of titanocene dichloride, a chemotherapeutic agent now in clinical trials. . . . . *Page 683*

Schuhmacher and colleagues report on a study in mice evaluating a novel bombesin analog labeled with ^{68}Ga for gastrin-releasing peptide receptor imaging with PET. . . . . *Page 691*

Pozzi and Zalutsky detail the results of experiments to identify the phenomena responsible for difficulties in ^{211}At-labeled antibody synthesis at high radiation doses and the solvent-related effects that may be relevant to synthesis of other therapeutic radiopharmaceuticals. . . . . *Page 700*

Aubert-Broche and colleagues compare and evaluate 4 methods for SPECT detection of interhemispheric asymmetries of brain perfusion in epilepsy, with special attention to the relative merits of quantitative assessment and visual inspection. . . . . *Page 707*

ON THE COVER

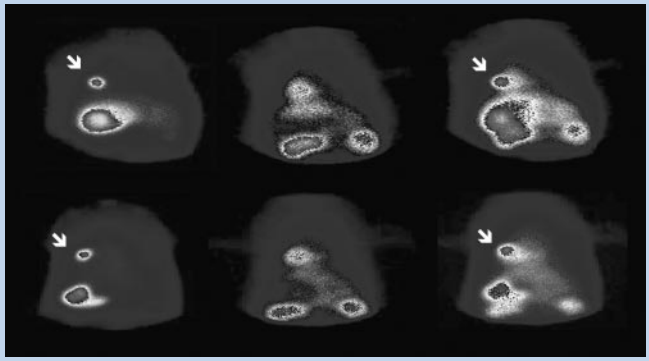

Because cardiac gene therapy entails multiple complex steps, including delivery and expression of transgenes, interest is increasing in noninvasive methods of monitoring myocardial gene expression. The need for PET scanners and on-site radiochemical synthesis limits widespread application of radioprobes that specifically target proteins produced by the transgene of interest. More accessible instruments and simple radioprobes have been under study, such as the use of γ-cameras and free radioiodide to study the sodium/iodide symporter (NIS) gene. A dual-gene vector that included the NIS gene as a reporter gene appeared to allow accurate assessment of the level of myocardial expression of a second gene of interest.